Crystal structure, phase transition, and magnetic ordering in perovskitelike $Pb_{2-x}Ba_xFe_2O_5$ solid solutions

Ivan V. Nikolaev,[1] Hans D'Hondt,[2] Artem M. Abakumov,[1,*] Joke Hadermann,[2] Anatoly M. Balagurov,[3] Ivan A. Bobrikov,[3] Denis V. Sheptyakov,[4] Vladimir Yu. Pomjakushin,[4] Konstantin V. Pokholok,[1] Dmitry S. Filimonov,[1] Gustaaf Van Tendeloo,[2] and Evgeny V. Antipov[1]

[1]*Department of Chemistry, Moscow State University, 119991 Moscow, Russia*

[2]*EMAT, University of Antwerp, Groenenborgerlaan 171, B-2020 Antwerp, Belgium*

[3]*Frank Laboratory of Neutron Physics, Joint Institute for Nuclear Research, 141980 Dubna, Russia*

[4]*Laboratory for Neutron Scattering, ETH Zurich and Paul Scherrer Institut (PSI), CH-5232 Villigen, Switzerland*

(Received 4 April 2008; published 23 July 2008)

The crystal and magnetic structures of the $x \approx 1$ member of the $Pb_{2-x}Ba_xFe_2O_5$ solid solution series have been studied using x-ray and neutron powder diffraction, electron diffraction, high-resolution electron microscopy, and Mössbauer spectroscopy. $Pb_{1.08}Ba_{0.92}Fe_2O_5$ has two polymorphic forms with the orthorhombic unit cell with $a \approx \sqrt{2}a_p$, $b \approx a_p$, and $c \approx 4\sqrt{2}a_p$ (a_p—the parameter of the perovskite subcell) with the *Pnma* space group of the low-temperature (LT) phase and the *Imma* space group of the high-temperature (HT) phase, which are related by a phase transition at $T_c \approx 540$ K. The crystal structures of both polymorphs were refined from neutron powder-diffraction data at $T=14$ K and $T=700$ K. The structure consists of parallel perovskite blocks with the thickness of two FeO_6 octahedra linked together by infinite chains of edge-sharing distorted FeO_5 trigonal bipyramids with two columns of the Pb cations in between characterized by the asymmetric coordination environment due to localized $6s^2$ lone electron pair. Two mirror-related configurations of the trigonal bipyramidal chains are ordered in the LT structure; their arrangement becomes disordered in the HT structure. Below $T_N=625$ K, $Pb_{1.08}Ba_{0.92}Fe_2O_5$ transforms into an antiferromagnetically ordered state. The antiferromagnetic (AFM) structure with a propagation vector $\mathbf{k}=[0,\frac{1}{2},\frac{1}{2}]$ is characterized by an antiparallel spin alignment for all nearest-neighbor Fe atoms in the perovskite blocks, which stack on to each other at the trigonal bipyramidal chains, resulting in alternating antiparallel and parallel arrangement of spins on going along the common edge of the FeO_5 trigonal bipyramids. An unusual spin flipping dynamic behavior was revealed by Mössbauer spectroscopy and related to a specific character of superexchange interactions inside the chains of the FeO_5 trigonal bipyramids.

DOI: 10.1103/PhysRevB.78.024426 PACS number(s): 61.66.Fn, 61.50.Ks, 75.25.+z

I. INTRODUCTION

It is generally assumed that accommodation of the cations with a lone $6s^2$ electron pair (Bi^{3+}, Pb^{2+}, etc.) in the *A* position of the perovskite ABO_3 structure leads to the structural instability toward an off-center displacement of the *A* cations caused by sterical activity of the lone pair and the covalent character of the bonding between the *A* cations and oxygen atoms.[1] Such displacements lead to ferroelectricity in perovskites $BiMnO_3$ and $BiFeO_3$, where the magnetic ordering also occurs due to the 3*d* transition metal cations at the *B* positions ($BiFeO_3$ is a spin canted antiferromagnet, with $T_{FE}=1083$ K and $T_N=673$ K; $BiMnO_3$ is a ferromagnet, with $T_{FE}=760$ K and $T_c=110$ K).[2,3] Significant attention has been paid to such multiferroic Bi-based perovskites where the spontaneous electric polarization and magnetic ordering are combined and numerous attempts were undertaken to expand the family of the Bi-based perovskites using syntheses at ambient and high pressures. However, little is known about similar perovskites in the Pb-Fe-O and Pb-Mn-O systems. The anion-deficient perovskites "$Pb_2Fe_2O_5$" and "$PbMnO_{2.75}$" have a complex structure due to fragmentation of the perovskite matrix by periodical translational interfaces [crystallographic shear (CS) planes].[4,5] A shear operation changes the connectivity scheme of the oxygen polyhedra around the *B* cation, transforming part of the corner-sharing BO_6 octahedra to chains of edge-sharing BO_5 tetragonal pyramids.[6] A fragmentation of the three-dimensional perovskite framework by CS planes into quasi-two-dimensional perovskite blocks and the presence of one-dimensional chains of edge-sharing BO_5 polyhedra can lead to unusual magnetic behavior related to reduced dimensionality and competitive superexchange interactions in the chains due to a presence of both ~180° and 90° *B*-O-*B* superexchange paths. Up to now limited information is available on the magnetic properties of the compounds with CS structures. It was only reported that the $Pb_2Fe_2O_5$ compound transforms into an antiferromagnetically ordered state below $T_N=555$ K.[7] The goal of the present work is to investigate the crystal and magnetic structures of the $Pb_{2-x}Ba_xFe_2O_5$ solid solutions with the simplest $(\bar{1}01)_p$ (the subscript index *p* stands for perovskite subcell) CS planes since these compounds can be considered as representative of other more complex CS structures in perovskites. We report a neutron-diffraction and Mössbauer spectroscopy study of the antiferromagnetic structure of $Pb_{1.08}Ba_{0.92}Fe_2O_5$ as well as an unusual spin dynamic behavior at temperatures close to T_N. A qualitative picture of superexchange interactions is provided to explain the experimental observations. A more detailed Mössbauer spectroscopy investigation of the magnetic behavior of the $Pb_{2-x}Ba_xFe_2O_5$ solid solutions will be published separately.

II. EXPERIMENT

The $Pb_{2-x}Ba_xFe_2O_5$ ($x=0.2-1.2$, $\Delta x=0.2$) samples were prepared by a solid-state reaction of PbO, Fe_2O_3, and $BaCO_3$ (Aldrich, 99.9% purity). Stoichiometric amounts of the initial materials were mixed in an agate mortar under acetone, pressed into pellets, and calcined at 750 °C in argon flow for 24 h. The reacted mixtures were then thoroughly reground and pressed into pellets. The pellets were annealed at 800 °C in argon flow for 100 h with three intermediate regrindings. A second set of samples in the above-mentioned compositional range was prepared in the same temperature regime in air.

X-ray powder-diffraction (XRD) data were collected with a Huber G670 Guinier diffractometer (Cu $K\alpha 1$ radiation, curved Ge monochromator, transmission mode, image plate). High-temperature XRD patterns were obtained with a Bruker D8 Advance powder diffractometer (Cu $K\alpha 1$ radiation, reflection mode).

Neutron powder-diffraction (NPD) experiments were carried out with the high-resolution powder diffractometer HRPT (wavelength $\lambda=2.45$ Å) with the use of the closed-cycle refrigerator at low temperature (14 K) and of the radiation-type furnace at high temperatures up to 700 K.[8] The NPD patterns were measured at $T=14$ K, in the range of $T=300-600$ K with the step of 30 K, and at $T=700$ K. The symmetry analysis of possible magnetic configurations has been carried out with the program SARAH-2K.[9] The crystal and magnetic structures were refined using a FULLPROF program package.[10] The atomic displacement parameters for all oxygen atoms were assumed isotropic and refined with constraint to equality.

Electron-diffraction (ED) studies were performed using a Phillips CM20 microscope and high-resolution electron microscopy (HREM) was done using a JEOL 4000EX instrument. Energy dispersive x-ray (EDX) spectra were obtained with the Phillips CM20 microscope equipped with an Oxford INCA system. The HREM images were simulated by means of the JEMS software.[11]

Mössbauer spectroscopy experiment (^{57}Fe) was performed in a transmission mode using a constant acceleration Mössbauer spectrometer coupled with a 1024 multichannel analyzer. A ^{57}Co/Rh γ-ray source was used for the experiments. The velocity scale was calibrated relative to α-Fe. All isomer shift values (δ) are referred to α-Fe. All experimental data were resolved in sets, with Lorentzian line shapes using an iterative least-squares fitting program.

The electron localization function (ELF) (Refs. 12 and 13) distribution was evaluated for $PbBaFe_2O_5$. To reveal the spatial ELF distribution, the density-functional theory (DFT) calculation of the electronic structure of $PbBaFe_2O_5$ was performed within the tight-binding–linear muffin-tin orbital–atomic-sphere approximation (TB-LMTO-ASA) approach (e.g., Ref. 14). A Barth-Hedin exchange-correlation potential was applied.[15] Pb($6s$,$6p$), Ba($6s$,$6p$), Fe($4s$,$4p$,$3d$), and O($2s$,$2p$) harmonics were used in the LMTO basis set directly; Pb($6d$,$5f$) and O($3d$) harmonics were obtained by using the downfolding technique. Despite the applied corrections for neglecting the interstitial regions and partial waves of higher order,[16] the addition of nine inequivalent empty spheres per unit cell was necessary. The calculation was performed for 24 k points in the irreducible wedge of the Brillouin zone (BZ). The integration over the BZ was performed by the tetrahedron method (144 inequivalent tetrahedra). The LMTO 4.7 program package was used for the calculation; the ELF distribution was revealed using the intrinsic procedure of this package.[17]

TABLE I. Unit-cell parameters for the $Pb_{2-x}Ba_xFe_2O_5$ solid solutions from room-temperature XRD data.

x	a (Å)	b (Å)	c (Å)	V (Å^3)
0.6	5.7597(2)	3.9724(2)	21.1371(7)	483.61(4)
0.8	5.7652(2)	3.9836(1)	21.1517(7)	485.79(4)
1.0	5.7689(3)	3.9944(2)	21.160(1)	487.60(7)

III. RESULTS AND DISCUSSION

A. Preparation and preliminary characterization

The single phase $Pb_{2-x}Ba_xFe_2O_5$ samples were obtained for $x=0.6$, 0.8, and 1.0. The powder XRD patterns were indexed on an orthorhombic lattice with unit-cell parameters $a\approx\sqrt{2}a_p$, $b\approx a_p$, and $c\approx 4\sqrt{2}a_p$ (a_p—the parameter of the perovskite subcell). These lattice parameters and the intensity distribution on the XRD patterns reflect the fact that this phase possesses a structure close to that of the $Pb_{1.33}Sr_{0.67}Fe_2O_5$ phase.[18] The homogeneity range of the $Pb_{2-x}Ba_xFe_2O_5$ solid solutions depends on the partial oxygen pressure during the thermal treatment. If the preparation was carried out in air, single phase samples of the $Pb_{2-x}Ba_xFe_2O_5$ solid solutions were obtained for $x=0.6$ and 0.8 only. The $Pb_{2-x}Ba_xFe_2O_5$ samples with higher Ba content ($x=1.0$, 1.2) contain impurities of $BaPbO_3$ and $BaFeO_{3-\delta}$, which indicates a partial oxidation. Annealing of the samples in Ar flow prevents oxidation and allows extension of the homogeneity range of the solid solutions up to $x=1.0$. The sample with $x=1.2$, prepared in Ar, contains an admixture of $BaFe_2O_4$ and is beyond the homogeneity range. For the samples with a Ba content below $x=0.6$, the formation of a mixture of the $Pb_{1.4}Ba_{0.6}Fe_2O_5$ and $Pb_2Fe_2O_5$ phases was observed. The cation compositions of these samples were confirmed by EDX analysis, which demonstrates Pb:Ba:Fe ratios close to those in the initial stoichiometries. The lattice parameters of these compounds are given in Table I. The lattice parameters and unit-cell volume increase monotonically with increasing Ba content, in agreement with the ionic radii of the Pb^{2+} and Ba^{2+} cations [$r(Ba_{XII})=1.60$ Å, $r(Pb_{XII})=1.49$ Å].[19]

The reflection conditions derived from the XRD patterns of the $Pb_{2-x}Ba_xFe_2O_5$ compounds ($0kl$, $k+l=2n$; $hk0$, $h=2n$) are in agreement with the *Pnma* space group; this space group was also assigned to the $Pb_{1.33}Sr_{0.67}Fe_2O_5$ crystal structure.[18] It should be noted, however, that the reflections with $h+k+l\neq 2n$ are systematically very weak and only a few of them were unambiguously detected. In order to reveal the true space symmetry, the samples were studied with electron diffraction. An investigation using XRD and NPD at

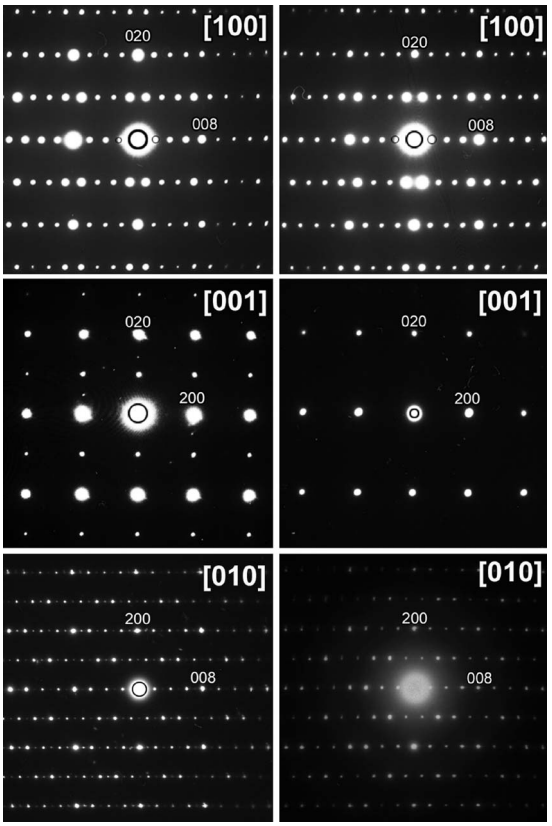

FIG. 1. The [100], [001], and [010] ED patterns of $PbBaFe_2O_5$: left column—room-temperature patterns; right column—the patterns of the HT phase.

different temperatures was performed as well in order to detect possible phase transitions.

B. Space symmetry and phase transition

The room-temperature electron-diffraction patterns of $PbBaFe_2O_5$ are shown in the left column of Fig. 1. The complete indexation of the ED patterns was performed using an orthorhombic unit cell with $a \approx 5.8$ Å, $b \approx 4.0$ Å, and $c \approx 21.2$ Å, as determined from the XRD data. The $0kl:k+l=2n$ and $hk0:h=2n$ reflection conditions are unambiguously derived from the [100], [001], and [010] ED patterns, in agreement with the proposed *Pnma* space group. The forbidden $h00:h \neq 2n$ and $00l:l \neq 2n$ reflections are visible on the [010] ED pattern. However, the absence of these reflections on the [100] and [001] ED patterns proves that they are caused by double diffraction. Thus the reflection conditions imposed by the *Pnma* space group are not violated.

Upon heating *in situ* inside the electron microscope, the ED patterns demonstrate weakening of the reflections with $h+k+l \neq 2n$ until their complete disappearance at ~410 K, which indicates a phase transition. The ED patterns of the high-temperature (HT) phase are shown in the right column of Fig. 1. The unit-cell parameters derived from these patterns remain the same as those for the low-temperature (LT) phase. However, the absence of the $h+k+l \neq 2n$ reflections suggests that the HT phase has a body-centered unit cell. Along with the reflection condition imposed by centering,

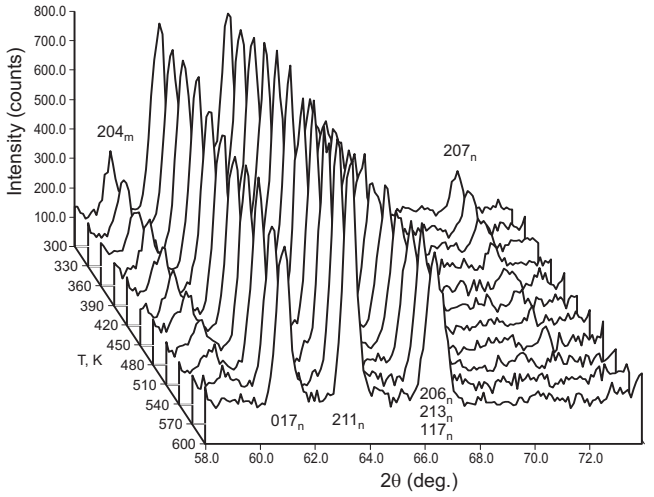

FIG. 2. NPD patterns of $PbBaFe_2O_5$ taken in the 300–600 K temperature range. Structural and magnetic phase transitions are marked by complete vanishing of the 204_m and 207_n reflections, respectively (*m* stands for the reflections of magnetic subsystem; *n* stands for nuclear reflections).

the $hk0:h$, $k=2n$ reflection condition was also observed and allows proposal of the *Imma* space group for the HT phase. The diffraction patterns of the LT phase are fully restored on cooling, demonstrating the reversibility of the phase transition. Thus, the LT and HT phases have the same $a \approx \sqrt{2}a_p$, $b \approx a_p$, $c \approx 4\sqrt{2}a_p$ unit cell but different space symmetries: *Pnma* for the LT phase and *Imma* for the HT phase.

The phase transition was also observed using high-temperature x-ray and neutron diffraction. Weak reflections violating the body centering become gradually broadened and decrease in intensity while the XRD pattern is observed upon heating, as was observed for the strongest (207) reflection. Due to the weakness of these spots, it is difficult to determine the transition temperature exactly from the XRD data. The NPD patterns provide more precise information on the transition temperature. Figure 2 demonstrates the evolution of the (207) reflection with temperature. The intensity of this reflection vanishes completely between 510 and 540 K, which delimits the possible range for the transition temperature. It should be noted that there is another reflection in this 2θ range at ~59°, shown in Fig. 2, which also vanishes with increasing temperature, but a complete suppression is achieved at 625 K. It will be shown further that this reflection originates from the antiferromagnetic ordering.

The transition temperature observed with NPD is higher than that observed with ED in the *in situ* heating experiment. This discrepancy can be caused by extra heating of the sample by the electron beam during the observations, which results in an underestimation of the transition temperature.

The group-subgroup relationship between the *Imma* and *Pnma* space groups allows the phase transition to be of second order. The temperature dependence of the unit-cell volume does not demonstrate any discontinuities at the transition temperature, which is in agreement with the second-order phase transition.

C. Crystal structures of the LT and HT phases

The crystal structures of the LT and HT phases were refined from NPD patterns at temperatures ranging from 14 to 700 K. The atomic coordinates of the $Pb_{1.33}Sr_{0.67}Fe_2O_5$ crystal structure were taken as an initial model for the LT phase with the *Pnma* symmetry. This model was transformed into the *Imma* symmetry, which gave the starting atomic positions of the HT phase. Careful inspection of the powder XRD pattern of the $PbBaFe_2O_5$ sample for the NPD experiment revealed the presence of a minor amount of the admixture phases $BaFe_2O_4$ and $BaFe_{12}O_{19}$ (2.0 and 0.7 wt %, respectively). The admixture phases were taken into account for the Rietveld refinements from the NPD data. The occupancy factors for the *A* positions in the perovskite block and in the six-sided tunnels were refined. The position in the six-sided tunnels is filled exclusively with Pb, whereas a mixed occupation by Pb and Ba was found for the *A* position in the perovskite block. The refined Pb contents were found to be 0.070(12) ($T=14$ K) and 0.086(16) ($T=700$ K). Since it is hardly possible to expect a variation of the Pb/Ba ratio with temperature at or below 700 K, the average occupancy factor of 0.92Ba+0.08Pb was assigned to the *A* position in the perovskite block, which corresponds to the $Pb_{1.08}Ba_{0.92}Fe_2O_5$ chemical formula. The observed Ba deficiency in comparison with the nominal $PbBaFe_2O_5$ composition agrees with the presence of the Ba-containing admixtures and can be explained by difficulties in the preparation of a fully homogeneous bulk sample at relatively low annealing temperature of 800 °C. The experimental, calculated, and difference NPD profiles for the $T=14$ K and $T=700$ K refinements are shown in Fig. 3. The crystallographic parameters of the LT phase at $T=14$ K and the HT phase at $T=700$ K are given in Table II. The main interatomic distances are listed in Table III.

The crystal structure of the LT form of the $Pb_{1.08}Ba_{0.92}Fe_2O_5$ phase is shown in Fig. 4. The corner-sharing $Fe2O_6$ octahedra form the perovskite blocks. These octahedra are linked through common corners to the double chains of edge-sharing $Fe1O_5$ distorted polyhedra, deviating from either the perfect trigonal bipyramidal shape or the tetragonal pyramidal shape. Formally, the $Fe1O_5$ polyhedron can be considered as a distorted trigonal bipyramid with the O4-O3-O5 triangular base parallel to the *a-c* plane and centered with the Fe1 atom and two O3 apices pointing in the $+b$ and $-b$ directions. The chains, running along the *b* axis, and the octahedra of the perovskite block delimit the six-sided tunnels where exclusively the Pb atoms are located. The Ba atoms occupy the cuboctahedral cavities in the perovskite blocks. The $Fe2O_6$ octahedra are distorted: the Fe2 atoms form two substantially longer bonds to the oxygens common to the octahedra and trigonal bipyramids (O4 and O5 in the LT structure).

Due to the presence of two-dimensional perovskite blocks in the structure, one can assume that the driving force for the structural phase transition could be essentially the same as for numerous three-dimensional ABO_3 perovskites, subjected to octahedral tilting distortion. Such distortion is dictated by a requirement to eliminate the geometrical mismatch between the *A*-O and *B*-O interatomic distances when the *A* cations are too small for the cuboctahedral cavities of the perovskite framework. The tendency of the perovskite structure to undergo a tilting distortion is reflected by the tolerance factor value $t<1$, where $t=(r_A+r_O)/\sqrt{2}(r_B+r_O)$ and r_A, r_B, and r_O are the ionic radii of the *A* and *B* cations and oxygen, respectively. Assuming the *A* position in the perovskite block to be occupied by Ba atoms only, one can calculate the tolerance factor to be equal to 1.04. Thus, at room temperature, where the distorted LT form is stable, there are no prerequisites for octahedral tilts in the perovskite blocks. In the LT phase the *Pnma* space group allows rotation of the octahedra only around the *b* axis; this rotation is fixed to zero by the m_a mirror plane of the *Imma* space group in the HT phase. The deviation of the Fe2-O2-Fe2 bond angle from 180° can be taken as a measure of rotation. However, this bond angle remains close to 180° in the range of 1–2 standard deviations for the whole temperature range from 14 to 700 K [179.3(6)° for $T=14$ K]. Consequently, octahedral tilting distortion of the perovskite block should be rejected as a possible reason for the phase transformation.

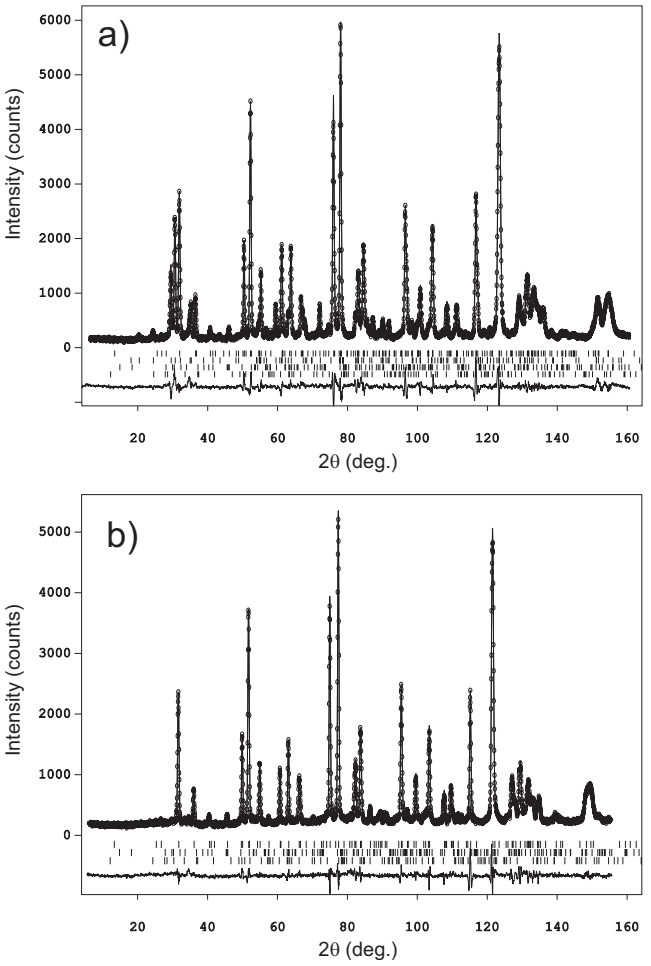

FIG. 3. Experimental, calculated, and difference NPD profiles for (a) LT ($T=14$ K) and (b) HT ($T=700$ K) $Pb_{1.08}Ba_{0.92}Fe_2O_5$ phases. Tick bars stand for (from top to bottom) (a) $Pb_{1.08}Ba_{0.92}Fe_2O_5$ (nuclear and magnetic contribution), $BaFe_2O_4$, $BaFe_{12}O_{19}$; and (b) $Pb_{1.08}Ba_{0.92}Fe_2O_5$, $BaFe_2O_4$, $BaFe_{12}O_{19}$.

Major structural changes with temperature occur in the geometry of the $Fe1O_5$ polyhedra. Figure 5 demonstrates the

TABLE II. The structural parameters for the LT and HT $Pb_{1.08}Ba_{0.92}Fe_2O_5$ phases, refined from NPD data.

	LT, $T=14$ K, *Pnma*	HT, $T=700$ K, *Imma*
a(Å)	5.75123(7)	5.80180(6)
b(Å)	3.97854(4)	4.02362(4)
c(Å)	21.1289(3)	21.2307(2)
Pb1, occupancy	4*c*, Pb	4*e*, Pb
x,y,z; B_{iso}(Å^2)	0.0032(8), 1/4, 0.5715(2); 0.1(1)	0, 1/4, 0.5713(2); 1.9(1)
Ba1, occupancy	4*c*, 0.92Ba+0.08Pb	4*e*, 0.92Ba+0.08Pb
x,y,z; B_{iso}(Å^2)	0.5133(15), 1/4, 0.6859(4); 0.1(1)	1/2, 1/4, 0.6841(4); 1.5(1)
Fe1, occupancy	4*c*, Fe	4*e*, Fe
x,y,z; B_{iso}(Å^2)	0.4789(10), 1/4, 0.4460(2); 0.15(5)	1/2, 1/4, 0.4458(2); 0.61(5)
Fe2, occupancy	4*c*, Fe	4*e*, Fe
x,y,z; B_{iso}(Å^2)	0.9793(8), 1/4, 0.3138(2); 0.15(5)	0, 1/4, 0.3126(2); 0.61(5)
O1, occupancy	4*c*, O	4*e*, O
x,y,z; B_{iso}(Å^2)	0.0142(13), 1/4, 0.6797(4); 0.05(5)	0, 1/4, 0.6779(4); 0.94(5)
O2, occupancy	4*c*, O	4*c*, O
x,y,z; B_{iso}(Å^2)	0.7285(15), 1/4, 0.2508(6); 0.05(5)	3/4, 1/4, 1/4; 0.94(5)
O3, occupancy	4*c*, O	8*i*, 0.5O
x,y,z; B_{iso}(Å^2)	0.5540(13), 1/4, 0.5390(3); 0.05(5)	0.468(2), 1/4, 0.5406(3); 0.94(5)
O4, occupancy	4*c*, O	8*i*, O
x,y,z; B_{iso}(Å^2)	0.2126(12), 1/4, 0.3906(5); 0.05(5)	0.2417(8), 1/4, 0.3905(2); 0.94(5)
O5, occupancy	4*c*, O	
x,y,z; B_{iso}(Å^2)	0.7318(13), 1/4, 0.3906(5); 0.05(5)	
R_B, R_P, R_{wP}	0.028, 0.069, 0.090	0.036, 0.063, 0.085

temperature dependence of the displacements of the Fe1 and O3 atoms in the LT structure from the $(x,0,0)$, $x=0$, 1/2 planes, which are the m_a mirror planes of the *Imma* space group (i.e., from their tentative positions in the HT structure). The displacement of the Fe1 atom gradually vanishes on heating until it becomes zero at $T_c \sim 540$ K. In the HT phase the Fe1 atom has an equilibrium position at the m_a plane. The behavior of the O3 atom is different. Its displacement also decreases monotonically with increasing temperature, but even above T_c this atom is not located exactly at the m_a plane but above or below along the a axis, occupying an eightfold position with halved occupancy. The x coordinate for this position does not vary significantly with temperature at $T>T_c$. Introducing these displacements into the refinement results in a significant improvement of the fit and decreases R_B from 0.049 to 0.036.

The displacements of the O3 atoms provide a key to understanding the nature of the phase transition. Due to absence of the m_a mirror plane and the asymmetrical shape of the six-sided tunnels in the LT phase, there are two strongly nonequivalent Pb1-O3 distances of 2.67 and 3.24 Å, so that one of the two Pb1-O3 separations is practically nonbonding (Fig. 6). At the same time, the asymmetry of the six-sided tunnel, which introduces the difference in the Pb1-O3 bond lengths, provides a space inside the tunnels where the lone $6s^2$ pair on the Pb1 atoms is localized. The localization of the lone pair is undoubtedly shown by the ELF isosurface (Fig. 7), which presents large lobes near the lead atoms. Such lobes are usually associated with sterically active (or, in other words, localized) $6s^2$ lone pairs. One can assume that this localization of the $6s^2$ lone pair should also retain in the HT structure.

In the LT structure, there are the double chains of the $Fe1O_5$ trigonal bipyramids which are mirror images of each other (Fig. 8). The presence of such mirror-reflected chains recalls the structural organization in the brownmillerites $A_2BB'O_5$, where the infinite parallel chains of the corner-linked $B'O_4$ tetrahedra also adopt two mirror-related configurations due to the opposite signs of rotations of the tetrahedra in the chains (see Fig. 2 of Ref. 20). Continuing the analogy with the brownmillerite structure, one can arbitrarily call the chains of the $Fe1O_5$ trigonal bipyramids with different configurations as "left" (L) and "right" (R). If the $[\frac{1}{2},\frac{1}{2},\frac{1}{2}]$ translation relates two chains transforming every $Fe1O_5$ pyramid into its mirror image, the chains are of different signs; otherwise, the chains are of the same sign. One possible arrangement of the L and R chains is realized in the LT phase: in *Pnma* space group the layers of the L chains alternate with the layers of the R chains. One can expect that the L chain can be transformed into an R chain and vice versa by small atomic displacements at low energy cost. Indeed, the symmetry operation relating the L and R chains is also a symmetry operation of the parent perovskite structure, so that the $L \leftrightarrow R$ transformation does not significantly disturb the perovskite blocks. Such transformation occurs via tiny atomic movements, which mainly involve a displacement of the O3 atom along the a axis (Fig. 8). Random displacements of the O3 atoms from the m_a plane experimen-

TABLE III. The main interatomic distances (Å) for the LT and HT $Pb_{1.08}Ba_{0.92}Fe_2O_5$ phases, refined from NPD data.

LT, $T=14$ K		HT, $T=700$ K[a]	
Pb1-O1	2.287(9)	Pb1-O1	2.263(9)
Pb1-O3	2.673(9)	Pb1-O3	2.79(1)×2
Pb1-O3	3.241(9)	Pb1-O3	3.16(1)×2
Pb1-O4	2.481(6)×2	Pb1-O4	2.583(9)×4
Pb1-O5	2.631(6)×2		
		Ba1-O1	2.930(12)
Ba1-O1	2.873(11)	Ba1-O1	2.9039(5)×2
Ba1-O1	2.884(11)	Ba1-O2	2.848(4)×4
Ba1-O1	2.842(12)	Ba1-O3	3.052(11)×2
Ba1-O2	2.772(10)×2	Ba1-O4	2.967(5)×4
Ba1-O2	2.837(10)×2		
Ba1-O3	3.111(11)	Fe1-O3	2.041(2)×4
Ba1-O4	3.002(9)×2	Fe1-O3	2.021(7)×2
Ba1-O5	2.924(9)×2	Fe1-O4	1.903(5)×2
Fe1-O3	2.023(1)×2	Fe2-O1	2.0219(9)×2
Fe1-O3	2.011(7)	Fe2-O2	1.967(3)×2
Fe1-O4	1.934(10)	Fe2-O4	2.169(5)×2
Fe1-O5	1.867(10)		
Fe2-O1	1.9944(7)×2		
Fe2-O2	1.979(12)		
Fe2-O2	1.963(12)		
Fe2-O4	2.097(10)		
Fe2-O5	2.159(10)		

[a]The actual number of the bonds to the O3 atom is twice smaller due to halved occupancy of the O3 position.

tally observed in the HT phase strongly suggest that the chains of different configuration are still present at $T>T_c$, but they are randomly distributed and do not form an ordered arrangement. Assuming this, one can derive the real coordination of the Fe1 and Pb1 atoms in the HT structure. Choosing one particular configuration of the chain and neglecting all interatomic distances formally observed due to its mirror image, it becomes clear that the Fe1 atoms remain situated in distorted trigonal bipyramids with d(Fe1-O3)=2.041(2) Å ×2, 2.021(7) Å, and d(Fe1-O4)=1.903(5) Å×2. The Pb1 atom is coordinated by one O1 atom [2.263(9) Å], one O3 atom [2.79(2) Å], and four O4 atoms [2.583(9) Å×4], which is virtually the same as the Pb1 coordination in the LT phase.

One can expect that there is relatively strong cooperative interaction between the chains in the *ab* plane mediated by the Pb atoms in the six-sided tunnels. Alternating L and R chains within the same layer is hardly expectable because it leads to unfavorable coordination environment of the Pb atoms. At the same time, changing the chain configuration

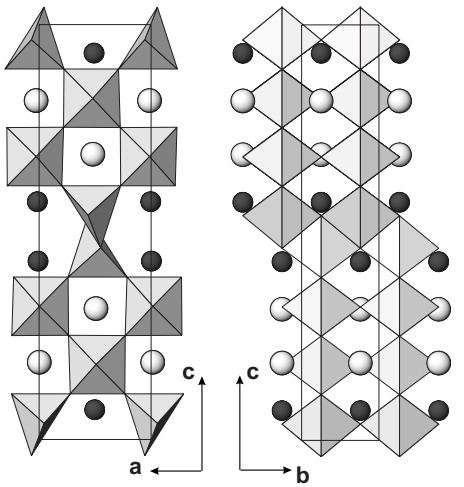

FIG. 4. The crystal structure of the LT $Pb_{1.08}Ba_{0.92}Fe_2O_5$ phase. The Fe atoms are situated in the shaded octahedra and distorted trigonal bipyramids. The Pb and Ba atoms are shown as dark and gray spheres.

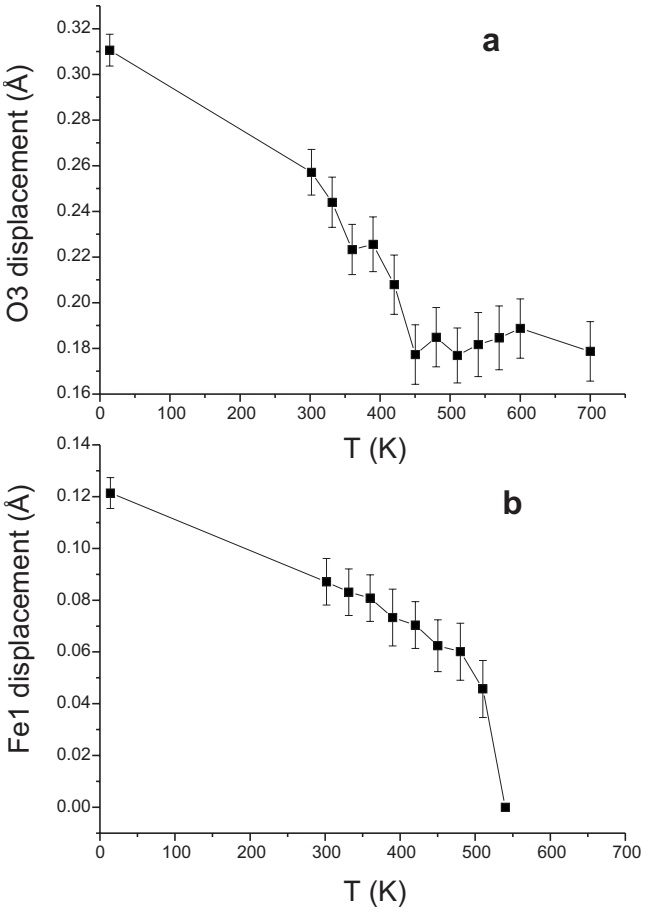

FIG. 5. Temperature dependences of the displacements of the (a) O3 and (b) Fe1 atoms from the $(x,0,0)$, $x=0$, 1/2 planes.

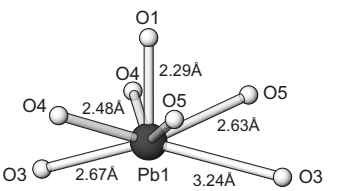

FIG. 6. Coordination environment of the Pb1 atoms in the low-temperature structure of $Pb_{1.08}Ba_{0.92}Fe_2O_5$.

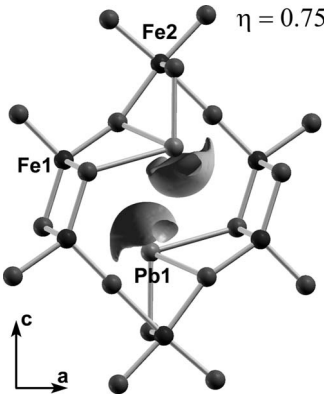

FIG. 7. ELF isosurface (η=0.75) for the LT $Pb_{1.08}Ba_{0.92}Fe_2O_5$ structure.

does not introduce significant strain in perovskite blocks, and a coupling between the chains in neighboring layers should be much weaker than the coupling within the layer. This suggests that in the HT phase there can be a two-dimensional order of the chains within the *ab* plane and a disordered stacking of the layers with chains of either L or R type along the *c* axis. This disorder can also have a dynamical nature.

Continuing the analogy with the brownmillerite structure, an extra model of the HT phase can be proposed. In such model with the *I*2*mb* space symmetry, all chains are of the same type (either L or R). The refinement with this model leads to R_B=0.039, higher than the R_B value for the *Imma* model. Moreover, the *x* atomic coordinates, which were fixed in the *Imma* model by the m_a mirror plane, demonstrate very large standard deviations in the *I*2*mb* structure. Thus, with the presently available data, we do not find reasons for symmetry lowering to *I*2*mb*, so all the refinements were done in the *Imma* model.

D. Defects associated with phase transition

A second-order phase transition results in fragmentation of the LT phase into domains which could be of orientational or translational origin.[21] The number of possible orientational domains is given by the ratio of the point-group orders of the HT and LT phase. Since both HT and LT phases possess the same point group *mmm*, orientational domains are not expected. Loss of the translational symmetry on going from the *Imma* to the *Pnma* space group will result in translational domains in the LT phase, where the structures on both sides of the domain wall are related by the $[\frac{1}{2},\frac{1}{2},\frac{1}{2}]$ vector lost at the phase transition. The volume ratio of the

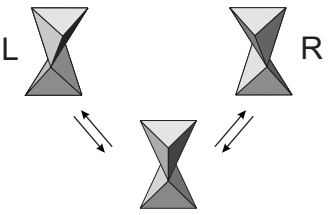

FIG. 8. L and R chains in the LT $Pb_{1.08}Ba_{0.92}Fe_2O_5$ structure and the scheme of their mutual transformation.

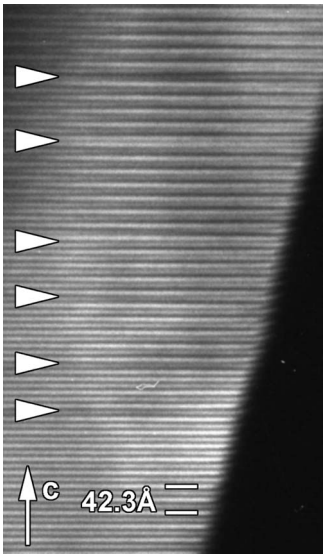

FIG. 9. Multibeam dark field image near the [010] zone showing antiphase boundaries in the LT $PbBaFe_2O_5$ structure.

primitive parts of the HT and LT phases is equal to 2, so that only two types of translational domains are possible with a single type of translational domain interface (antiphase boundary). Visualization of the antiphase boundaries was performed using multibeam dark field imaging with the crystal oriented nearly along the [010] zone axis. The crystal was tilted away from the perfect zone axis orientation in order to maximize the intensity of the triplet consisting of the *h*0*l*, *h*0*l*+1, and *h*0*l*+2 spots, where $h+l=2n$. These three spots were then selected for image formation. The resulting image demonstrates a sequence of stripes of different brightnesses, where the bright and less bright stripes alternate with an average periodicity of ~21 Å, which is the repeat period along the *c* axis. The alternation sequence is occasionally violated by the antiphase boundaries, which create two stripes of equal brightness located at *c*/2 distance with respect to each other (Fig. 9). The antiphase boundaries are strictly confined to the *ab* plane. It seems that at the observation conditions, they do not significantly interact with each other to produce any noticeable diffuse intensity.

E. LT and HT phases: HREM observations

High-resolution electron microscopy (HREM) images along the [010] zone were taken in order to visualize the structure in detail. It should be taken into account that severe beam heating occurs during the HREM experiment, which causes the transition to the HT phase. In order to control the effect of beam heating and acquire a clear image of the LT phase, low intensity images were taken, i.e., with a spread beam [Fig. 10(a)]. The Fourier transform of this image is set in the right upper corner and shows clearly the presence of the $h0l: h+l\neq 2n$ reflections characteristic for the *Pnma* symmetry. The unit cell is indicated by a black border. A calculated image using the structure data for the LT phase from Table II is included in the image, indicated by a white border. The best agreement was found for a focus value of

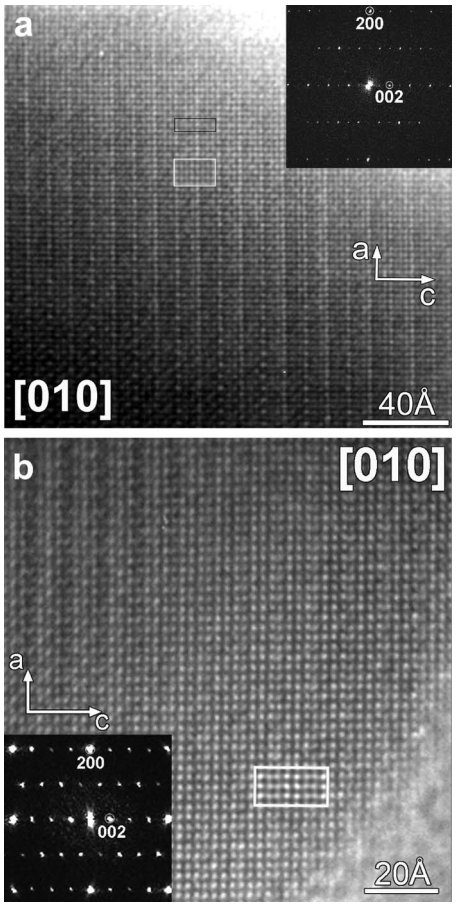

FIG. 10. (a) Low intensity HREM image of the [010] zone of the LT phase; (b) HREM image of the [010] zone of the HT phase. A calculated image is indicated by a white border. The unit cell is indicated in black and the Fourier transform is included.

$f=-150$ Å and the thickness $t=32$ Å. Under these imaging conditions, the brighter dots correspond to the Pb columns and the less bright dots correspond to the columns of Ba and Fe projected together with oxygen.

Figure 10(b) shows the HREM image of the [010] zone of the HT phase. This image was obtained by using normal conditions for high-resolution imaging, i.e., with enough beam heating to induce the phase transition. The Fourier transform of this picture is set in the left bottom corner and shows clearly the extinction of the $h+l\neq 2n$ spots, in agreement with the structure of the HT phase. A calculated image using the structure data for the HT phase from Table II is included in the image, surrounded by a white border. The best agreement between the calculated and the experimental image was found for a focus value of $f=-200$ Å and the thickness $t=40$ Å. Again the bright dots correspond to the cations, with the brightest ones being the Pb columns and the less bright ones being the columns of Ba and Fe.

F. Magnetic structure: neutron-diffraction and Mössbauer spectroscopy

Below the magnetic transition temperature of ~625 K, the neutron-diffraction patterns contain a set of superstructure reflections, which are not located at the positions of the nuclear-cell calculated reflections. These reflections monotonically increase in intensity with decreasing temperature, indicating the onset of the long-range antiferromagnetic ordering (Fig. 11).

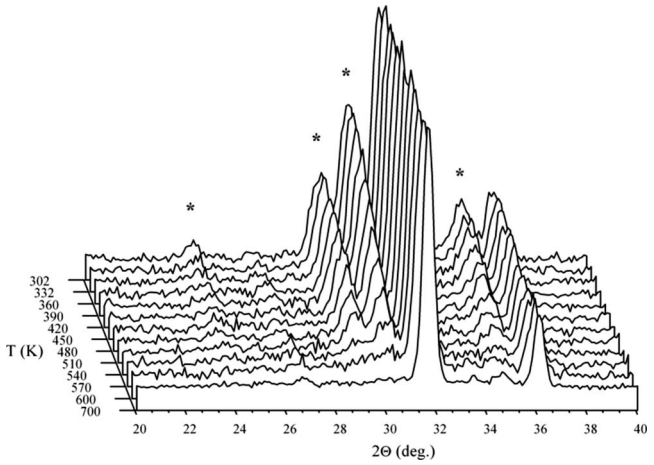

FIG. 11. Parts of the neutron-diffraction patterns of $Pb_{1.08}Ba_{0.92}Fe_2O_5$ measured at different temperatures with the HRPT diffractometer ($\lambda=2.45$ Å). The intensity of the superstructural peaks marked with asterisks decreases with increasing temperature, indicating the antiferromagnetic transition.

The whole set of the magnetic diffraction peaks is indexed with the propagation vector $\mathbf{k}=[0,\frac{1}{2},\frac{1}{2}]$. Using the determined propagation vector, we performed the symmetry analysis according to Izyumov *et al.*[22] in order to derive the possible magnetic configurations for both Fe (4*e*) sites of the space group *Imma*. The decompositions of the magnetic representations for both the Fe1 and the Fe2 sites are listed in the Table IV. The trial magnetic structure models were constructed for all the irreducible representations $\Gamma_1,\ldots,\Gamma_4$ and tested with the Rietveld refinements under two assumptions: (1) both the Fe1 and Fe2 magnetic ions order with one and the same irreducible representation (IR) and (2) the mixing coefficients for the basis vectors have to be constrained in such a way that both the Fe1 and Fe2 magnetic ions possess constant and equal magnetic-moment magnitudes. It turns out that the ideal description of the profile is only achieved with the irreducible representation Γ_3 with the basis vectors corresponding to the magnetic-moment directions along the crystallographic axes *b* and *c*. The component of the magnetic moment along the *b* axis is dominant, and the symmetry-allowed component along the *c* axis is minor (about ten times weaker), so that the resulting magnetic Fe moments are directed almost ideally along the crystallographic axis *b* of the parent crystallographic unit cell. As the compound undergoes a transition from *Imma* to *Pnma* symmetry at about 540 K on cooling, no peculiarities are observed in the behavior of the magnetic intensities—they simply continue increasing as if the magnetic structure would remain the same. The symmetry analysis carried out for the low-temperature structure proves that the found magnetic structure is also symmetry allowed for the low-temperature *Pnma* structure. This is why we consider the magnetic structure in the whole temperature range below the magnetic tran-

TABLE IV. Characters and basis vectors (BV) of the irreducible representations $\Gamma_1^1,\ldots,\Gamma_4^1$ of the little group of propagation vector $k=[0,\frac{1}{2},\frac{1}{2}]$ for the space group *Imma*. The decompositions of the axial vector representations for either of the 4*e* sites (Fe1 and Fe2) read as $\Gamma_{\mathrm{Mag}}=1\Gamma_1^1+1\Gamma_2^1+1\Gamma_3^1+1\Gamma_4^1$. The atoms of the nonprimitive basis are defined as 1: (0, $\frac{1}{4}$, 0.0542), 2: (0, $\frac{3}{4}$, 0.9458) and 1: (0, $\frac{1}{4}$, 0.3127), 2: (0, $\frac{3}{4}$, 0.6873) for the Fe1 and Fe2 sites, correspondingly.

Characters of the irreducible representations				
IR/symmetry operation	$2(x,0,0)$	$\bar{1}$	$m(0,y,z)$	
Γ_1	1	1	1	
Γ_2	1	−1	−1	
Γ_3	−1	1	−1	
Γ_4	−1	−1	1	
Basis vectors of the irreducible representations				
Atom/IR	Γ_1	Γ_2, Γ_2'	Γ_3, Γ_3'	Γ_4
1	100	010, 001	010, 001	100
2	100	$0\bar{1}0$, $00\bar{1}$	010, 001	$\bar{1}00$

sition at $T_N\approx 625$ K to be the same—in the low-temperature phase with the *Pnma* symmetry, the magnetic Fe1 and Fe2 ions are just slightly moving away from their symmetry positions of the high-temperature *Imma* structure. The illustration of the magnetic ordering scheme is given in Fig. 12, together with the crystal structure of the low-temperature phase, drawn in the left half of Fig. 12 in the same scale. One sees that the full magnetic unit cell is doubled with respect to the nuclear one in both the *b* and *c* directions (for clarity, the crystal structure unit-cell edges are plotted with thin lines within a magnetic unit cell). In the large Fe1-Fe2-Fe2-Fe1 blocks of the corner-sharing polyhedra, the ordering type is simple antiferromagnetic, with the magnetic Fe moments being aligned almost along the *b* axis of the crystal structure unit cell and coupled antiferromagnetically with respect to all the nearest Fe neighbors, i.e., along all $\langle 100\rangle_p$ directions of the perovskite subcell. These blocks (marked as AFM in the Fig. 12) are stacked at the chains of the $Fe1O_5$ trigonal bipyramids. Two different exchange paths exist along the chain: through the nearly straight Fe1-O3-Fe1 chains along the *b* axis (J_1) with the Fe1-O3-Fe1 angles varying between ~158° and ~165° at different temperatures and through the zigzag Fe1-O3-Fe1 chains (across the common edge of the pyramids) (J_2) with the Fe1-O3-Fe1 angles varying between ~97° and ~92° at different temperatures [see Fig. 16(a)]. The coupling of the magnetic Fe1 moments along the nearly straight Fe1-O3-Fe1 chains is always antiparallel, whereas the parallel and antiparallel couplings alternate along the zigzag Fe1-O3-Fe1 chains.

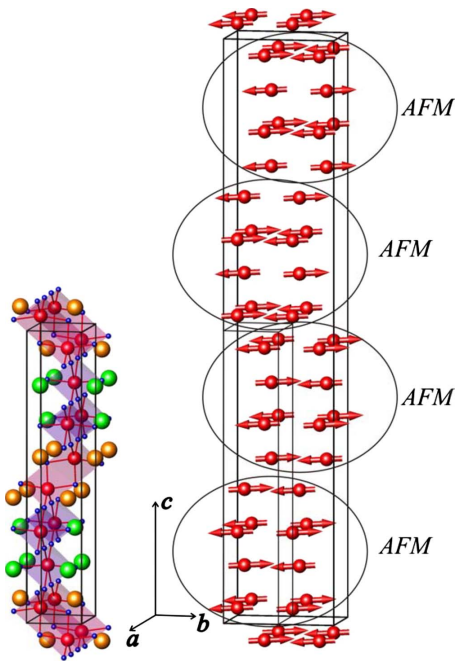

FIG. 12. (Color online) Illustration of the antiferromagnetic ordering scheme for the $Pb_{1.08}Ba_{0.92}Fe_2O_5$ compound (right half of the figure). The crystal structure of the low-temperature form of $Pb_{1.08}Ba_{0.92}Fe_2O_5$ is shown in the left in the same scale.

The saturated magnetic Fe moment at $T=14$ K is refined to $\mu=3.91(4)\mu_B$. This value of the long-range ordered magnetic Fe^{3+} moment is an indication that a significant part of the Fe^{3+} ions in the investigated compound is in the HS state ($\mu_{\mathrm{theor}}=5\ \mu_B$). The refined magnitudes of the ordered Fe

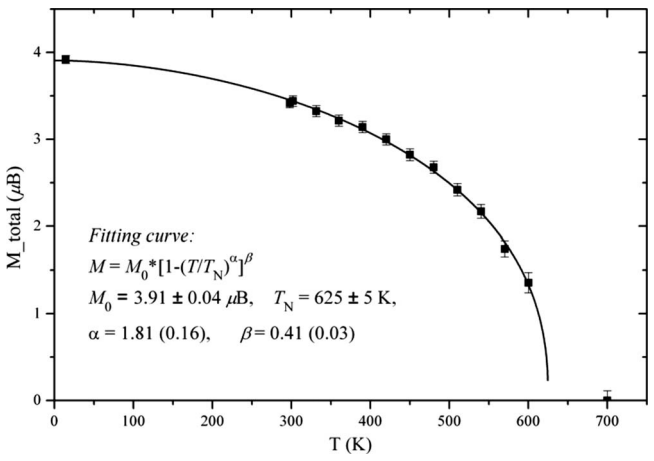

FIG. 13. Temperature dependence of the ordered magnetic Fe moment magnitude. The solid line is a fitting curve; details are discussed in the text.

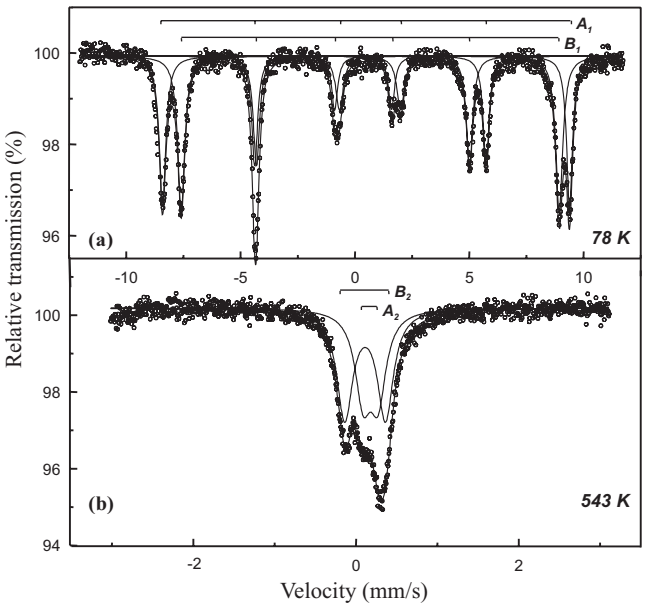

FIG. 14. ^{57}Fe Mössbauer spectra of $PbBaFe_2O_5$ recorded at (a) 78 and (b) 543 K.

magnetic moments are plotted against T in the Fig. 13. The M(Fe) data in Fig. 13 were fitted to an empirical formula: $M(T)=M_0[1-(T/T_N)^{\alpha}]^{\beta}$, with four refineable parameters: M_0—the saturated magnetic moment at $T=0$; T_N—the Néel temperature; and α and β—the refineable exponential parameters. The fit, which is shown as a solid line in the Fig. 13, yields the antiferromagnetic transition temperature of $T_N=625\pm5$ K.

The Mössbauer spectrum of $PbBaFe_2O_5$ measured at 78 K is shown in Fig. 14(a). The spectrum is composed of two Zeeman sextets, A_1 and B_1, of nearly equal contributions (Table V). The observed values of isomer shift IS $=0.4-0.5$ mm/s correspond to Fe^{3+} cations exclusively.[23] The A_1 sextet with higher values of both IS (0.51 mm/s) and the magnetic hyperfine field H_{hf} (54 T) can be assigned to octahedrally coordinated positions (Fe2 sites in Table II). The hyperfine parameters of the A_1 sextet are similar to those reported in literature for Fe^{3+} cations in octahedral sites of $Me_2Fe_2O_5$ (Me=Ca, Sr) brownmillerites.[24,25] The B_1 sextet is characterized by smaller values of IS=0.44 mm/s and $H_{hf}=50$ T, consisting of fivefold coordination of Fe1 sites (Table II). Note that the obtained IS value for the B_1 sextet is comparable to the few data reported in the literature for the fivefold coordinated Fe^{3+} cations and is in the range of ISs observed for octahedral and tetrahedral Fe^{3+} cations in oxides.[22–24] The observed area ratio of A_1 to B_1 sextets (1:1) is in good agreement with the structure refinement data (Table II).

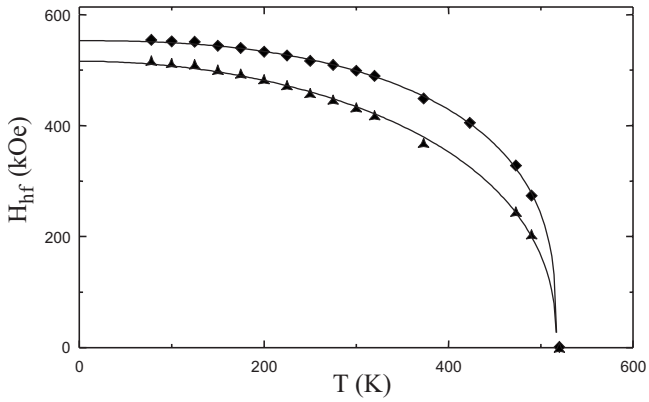

FIG. 15. Temperature dependence of the hyperfine field at ^{57}Fe in octahedral (♦) and fivefold coordinated (▲) sites of $PbBaFe_2O_5$.

Although the magnetic transition temperature of $PbBaFe_2O_5$ was found to be ~625 K, as determined by NPD, no magnetic splitting was observed in Mössbauer spectra obtained at temperatures above of 520 K. Figure 15 shows the temperature dependence of the H_{hf} for two subspectra corresponding to octahedral and fivefold coordinated Fe^{3+} cations. Figure 14(b) represents the spectrum of $PbBaFe_2O_5$ taken at 543 K, which was fitted with two A_2 and B_2 doublets of near equal areas with parameters listed in Table V. According to their IS values, the A_2 doublet is attributed to the octahedral positions (Fe2 sites in Table II), and the B_2 doublet—to the fivefold coordinated ones (Fe1 sites in Table II). Note that the phase transition to the *Pnma* LT phase at temperatures of ~500–540 K (see above) does not allow the parameters of quadrupole splitting Δ, obtained in the paramagnetic region, to be directly used to fit the magnetically split low-temperature spectra. A more detailed Mössbauer study of $PbBaFe_2O_5$ will be published elsewhere.

The observed temperature dependence of H_{hf} and the vanishing of the magnetic splitting at temperatures much below the magnetic transition temperature, determined by NPD, can be presumably related to a fast flipping of the magnetic moments of the Fe^{3+} cations, where the relaxation time is shorter than the ^{57}Fe Mössbauer spectroscopy time scale ($\sim10^{-7}$ s). A fluctuation of the hyperfine field due to spin

TABLE V. The ^{57}Fe Mossbauer hyperfine parameters of $PbBaFe_2O_5$ at 78 and 543 K: IS, isomer shift relative to α-Fe; ε, apparent quadrupole shift (at 78 K) calculated from $(v_6-v_5-(v_2-v_1))/4$; Δ, quadrupole splitting (at 543 K); H_{hf}, magnetic hyperfine field; Γ, linewidth; I, relative area.

T (K)	Component	IS $\pm$ 0.03 (mm/s)	$2\varepsilon\pm0.03$ (mm/s)	$\Delta\pm0.03$ (mm/s)	$H_{hf}\pm0.5$ (T)	$\Gamma\pm0.03$ (mm/s)	$I\pm2$ (%)
78	A_1	0.51	−0.2		54.2	0.33	48
	B_1	0.44	0.32		50.1	0.35	52
543	A_2	0.17		0.18		0.24	45
	B_2	0.11		0.5		0.24	55

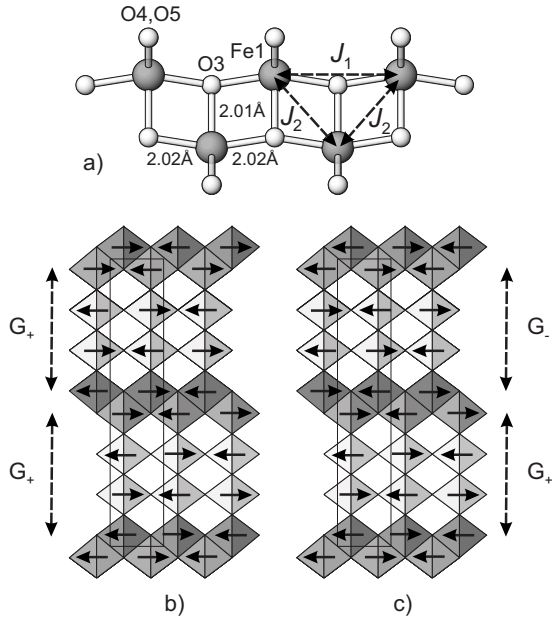

FIG. 16. (a) Superexchange Fe^{3+}-O-Fe^{3+} paths along the chain of the $Fe1O_5$ trigonal bipyramids: ~180° path J_1 and ~90° path J_2; the [100] structure projections showing two possible spin configurations (b) G_+-G_+ and (c) G_+-G_-. The crystallographic unit cell is outlined.

flipping occurs in the magnetic particles of finite size, where the magnetic anisotropy energy may become comparable with the energy of thermal agitation. However, this effect is strongly size dependent and relevant for the particles not larger than a few tens of nanometers (see Ref. 26 and references therein), which is definitely not the case for the $PbBaFe_2O_5$ sample, prepared by high-temperature solid-state reaction and demonstrating coarse crystalline structure. One can assume that the unusual magnetic dynamic behavior is an intrinsic feature of the $PbBaFe_2O_5$ magnetic structure due to significantly different superexchange interactions within the blocks of corner-sharing Fe-O polyhedra and between the adjacent blocks across the common edges of the $Fe1O_5$ trigonal bipyramids. Spin alignment in the large Fe1-Fe2-Fe2-Fe1 blocks of the corner-sharing polyhedra is governed by strong 180° antiferromagnetic (AFM) Fe^{3+}-O-Fe^{3+} superexchange (SE) paths between the iron atoms in the octahedral units as well as by nearly ~180° AFM SE path J_1 along the chains of the $Fe1O_5$ trigonal bipyramids [Fig. 16(a)], which results in a G-type AFM structure.[27,28] The stacking of the blocks occurs via much weaker ~90° SE paths J_2 [Fig. 16(a)], which results in magnetic frustration: parallel and antiparallel spin couplings are assigned to the J_2 SE paths equivalent by crystal symmetry. Choosing one Fe1-Fe2-Fe2-Fe1 block as a reference (G_+), spin flipping in the adjacent block does not alter the spin alignment along the chains of the $Fe1O_5$ trigonal bipyramids. Thus two possible spin configurations, G_+-G_+ and G_+-G_- [Figs. 16(b) and 16(c)], should be virtually energetically equivalent and thermally induced fast switching between them can cause vanishing of the magnetic splitting on the Mössbauer spectra. The temperature at which the magnetic splitting vanishes coincides with the critical temperature of the structural *Pnma-Imma* phase transition, which indicates possible involvement of the L↔R trigonal bipyramidal chain disorder in the magnetic dynamic behavior.

IV. CONCLUSIONS

Based on the crystal and magnetic structures of the $Pb_{2-x}Ba_xFe_2O_5$ solid solutions, estimates can be made on the possible features of the magnetic structure of $Pb_2Fe_2O_5$. Both $Pb_{2-x}Ba_xFe_2O_5$ and $Pb_2Fe_2O_5$ can be considered as CS structures where the perovskite matrix is periodically fragmented by the $(\bar{1}01)_p$ CS planes in $Pb_{2-x}Ba_xFe_2O_5$, whereas the $(104)_p$ planes are the most common in the $Pb_2Fe_2O_5$ sample corresponding to the $Pb_{15}Fe_{16}O_{39}$ actual composition.[4,6,29] The perovskite blocks on both sides of the CS plane are related by $\mathbf{R}=\frac{1}{2}[110]_p$ displacement vector. In both cases the double chains of FeO_5 trigonal bipyramids are the main constituting elements of the CS planes separating the perovskite blocks. $Pb_2Fe_2O_5$ transforms into antiferromagnetically ordered state below $T_N=555$ K.[7] However, up to now the computation of the crystal and magnetic structures is not performed due to high concentration of defects and intermixing areas with different types of the CS planes in this material.[29] However, it is reasonable to assume that antiferromagnetic order with antiparallel spin alignment for all nearest-neighbor Fe atoms will be realized in the perovskite blocks. The spin arrangement in the double chains of FeO_5 trigonal bipyramids can be also similar to that in $Pb_{2-x}Ba_xFe_2O_5$ because it corresponds to a match of two AFM perovskite blocks: antiparallel spins along the 180° interactions in the straight Fe-O-Fe chains and alternating antiparallel and parallel arrangement along the 90° interactions in the zigzag Fe-O-Fe chains.

ACKNOWLEDGMENTS

We are grateful to A. A. Tsirlin for help with ELF computation. This work was supported by the Russian Foundation of Basic Research (RFBR) (Grants No. 07-03-00664-a, No. 06-03-90168-a, No. 05-03-34812-MF-a, and No. 06-02-16032a). This work was supported in part by the IAP VI program of the Belgian government. This work was partially based on the experiments carried out at the Swiss spallation neutron source SINQ at the Paul Scherrer Institut, Villigen, Switzerland.

*Corresponding author.

[1] D. I. Khomskii, J. Magn. Magn. Mater. **306**, 1 (2006).
[2] I. Sosnowska, Ferroelectrics **79**, 127 (1988).
[3] T. Atou, H. Chiba, K. Ohoyama, Y. Yamaguchi, and Y. Syono, J. Solid State Chem. **145**, 639 (1999).
[4] A. M. Abakumov, J. Hadermann, S. Bals, I. V. Nikolaev, E. V. Antipov, and G. Van Tendeloo, Angew. Chem., Int. Ed. **45**, 6697 (2006).
[5] C. Bougerol, M. F. Gorius, and I. E. Grey, J. Solid State Chem. **169**, 131 (2002).
[6] A. M. Abakumov, J. Hadermann, G. Van Tendeloo, and E. V. Antipov, J. Am. Ceram. Soc. **91**, 1807 (2008).
[7] J.-C. Grenier, M. Pouchard, and P. Hagenmuller, Rev. Chim. Miner. **14**, 515 (1977).
[8] P. Fischer, G. Frey, M. Koch, M. Könnecke, V. Pomjakushin, J. Schefer, R. Thut, N. Schlumpf, R. Bürge, U. Greuter, S. Bondt, and E. Berruyer, Physica B **276-278**, 146 (2000).
[9] A. S. Wills, Physica B **276-278**, 680 (2000); program available from www.ccp14.ac.uk.
[10] J. Rodríguez-Carvajal, Physica B (Amsterdam) **192**, 55 (1993).
[11] P. Stadelmann, JEMS Java Electron Microscopy Software. Available from http://cime/www.epfl.ch/people/stadelmann/jemsWebSite/jems.html, 2005.
[12] A. D. Becke and K. E. Edgecombe, J. Chem. Phys. **92**, 5397 (1990).
[13] M. Kohout, Int. J. Quantum Chem. **97**, 651 (2004).
[14] P. Weinberger, I. Turek, and L. Szunyogh, Int. J. Quantum Chem. **63**, 165 (1997).
[15] U. Barth and L. Hedin, J. Phys. C **5**, 1629 (1972).
[16] O. K. Andersen, Phys. Rev. B **12**, 3060 (1975).
[17] O. Jepsen, A. Burkhardt, and O. K. Andersen, *The TB-LMTO-ASA Program, Version 4.7* (Max-Planck-Institut für Festkörperforschung, Stuttgart, 1999).
[18] V. Raynova-Schwarten, W. Massa, and D. Z. Babel, Z. Anorg. Allg. Chem. **623**, 1048 (1997).
[19] R. D. Shannon, Acta Crystallogr., Sect. A: Cryst. Phys., Diffr., Theor. Gen. Crystallogr. **32**, 751 (1976).
[20] A. M. Abakumov, A. S. Kalyuzhnaya, M. G. Rozova, E. V. Antipov, J. Hadermann, and G. Van Tendeloo, Solid State Sci. **7**, 801 (2005).
[21] G. Van Tendeloo and S. Amelinckx, Acta Crystallogr., Sect. A: Cryst. Phys., Diffr., Theor. Gen. Crystallogr. **30**, 431 (1974).
[22] Y. A. Izyumov, V. E. Naish, and R. P. Ozerov, *Neutron Diffraction of Magnetic Materials* (Consultants Bureau, New York, 1991).
[23] F. Menil, J. Phys. Chem. Solids **46**, 763 (1985).
[24] I. A. Leonidov, M. V. Patrakeev, J. A. Bahteeva, K. V. Poholok, D. S. Filimonov, K. R. Poeppelmeier, and V. L. Kozhevnikov, J. Solid State Chem. **179**, 3045 (2006).
[25] A. Sobolev, I. Presnyakov, K. Pokholok, V. Rusakov, T. Gubaidulina, A. Baranov, and G. Demazeau, Bull. Russ. Acad. Sci. Phys. **71**, 1314 (2007).
[26] S. Mørup, D. E. Madsen, C. Frandsen, C. R. H. Bahl, and M. F. Hansen, J. Phys.: Condens. Matter **19**, 213202 (2007).
[27] J. B. Goodenough, J. Phys. Chem. Solids **6**, 287 (1958).
[28] J. Kanamori, J. Phys. Chem. Solids **10**, 87 (1959).
[29] J. Hadermann, A. M. Abakumov, I. V. Nikolaev, E. V. Antipov, and G. Van Tendeloo, Solid State Sci. **10**, 382 (2008).